Exploring Semi-solid Deformation with the Discrete Element Method and Synchrotron Radiography

T.C. Su[1], C. O'Sullivan[2], T. Nagira[3], H. Yasuda[4] and C.M. Gourlay[1]
[1] Department of Materials, Imperial College, London SW7 2AZ, UK
[2] Department of Civil and Environmental Engineering, Imperial College, London SW7 2AZ, UK
[3] Department of Adaptive Machine Systems, Osaka University, 2-1 Yamadaoka, Suita, Osaka 565-0871, Japan
[4] Department of Materials Science and Engineering, Kyoto University, Yoshida-Honmachi, Sakyo-ku, Kyoto 606-8501, Japan

Abstract

Thin samples of equiaxed Al-8 wt.% Cu at 66 vol.% solid have been deformed in-situ using synchrotron radiography and quantified using digital image correlation (DIC). Discrete element method (DEM) simulations on a similar microstructure, deformation mode and boundary conditions were then performed to gain a deeper insight into the deformation processes. In both the experiments and simulations, there is reasonable agreement in the changes in local solid fraction due to shear-induced dilation and compaction, in the region where plastic deformation of grains occurred, and in the location and extent of strain localisation.

Keywords: Rheology, Synchrotron radiation, Discrete element method.

1. Introduction

Semi-solid alloy rheology is important in the feeding of solidification shrinkage [1] and the formation of defects such as macrosegregation [2-5], porosity and hot tearing [6, 7] and also plays a key role in pressurised processes such as semi-solid processing [8, 9], high-pressure die casting [5] and twin-roll casting [10, 11]. In these latter processes, defects have been related to the positive volumetric strain observed in the shear deformation of semi-solid alloys [12, 13] and can be linked to the shear-induced dilation phenomenon in granular (i.e. particulate) materials, known as Reynolds' dilatancy [14]. In the last decade, direct evidence of granular deformation such as shear-induced dilation and arching has been revealed in semi-solid alloys using real-time synchrotron X-ray imaging by thin-sample radio-graphy [15-20] and bulk-sample tomography [21, 22].

These granular deformation phenomena suggest that the particulate discrete element method (DEM) can be a useful approach to investigate semi-solid alloy deformation because it has been widely used to simulate deformation in granular matter such as soil mechanics [23] and powder metallurgy [24, 25]. A few studies have also applied DEM to semi-solid alloy deformation previously [7, 26].

This paper aims to demonstrate how coupling thin-sample deformation experiments with 2D DEM simulations can help to gain insights into semi-solid deformation. In-situ X-ray observation of direct shear at 66% solid is first quantified. The experiment is then reproduced in DEM simulation work, in which the grain size distribution, deformation mode and boundary conditions were set to be close to the experiment. The similarities and differences between the experiment and simulation are then discussed.

2. Methods

Samples were produced by casting an Al-8Cu-0.05Ti-0.01B (mass %) alloy with equiaxed dendritic microstructure. A slice with dimensions 10.0 mm × 7.5 mm and thickness 180-200 μm was prepared from the casting. Then, the sliced alloy was placed in the 200 μm thick cavity between two Al_2O_3 windows, as shown in Figure 1. Further, two BN plates were set to fix the window and mould. Experiments were conducted on beamline BL20B2 at the SPring-8 synchrotron in Hyogo, Japan, using apparatus described previously [18]. An X-ray beam with energy 16keV was set to transmit through the thin-plate sample and was collected by a high-resolution X-ray imaging detector. Signals within the observation area of 5.1 × 5.1 mm were digitised to 2048 × 2048 pixel format with 16-bit depth, and the pixel size was 2.5 × 2.5 μm.

Shear deformation was applied by the constant upward displacement of a mobile Al_2O_3 push plate, as shown in Figure 1.

The deformation experiment was conducted isothermally in the furnace, leading to a constant nominal solid fraction throughout the sample with a vacuum pressure of 10 Pa. The Al_2O_3 push-plate displacement rate in the vertical component du_y/dt was 28.80 μm/s upwards, and the horizontal displacement rate du_x/dt was 3.66 μm/s to the right. The volume fraction of solid g_S prior to deformation was 0.66, which was calculated from the transmission intensity through 100% liquid, I_L, 100% solid, I_S, and the semi-solid mixture, I_{SL} as suggested in reference [15]:

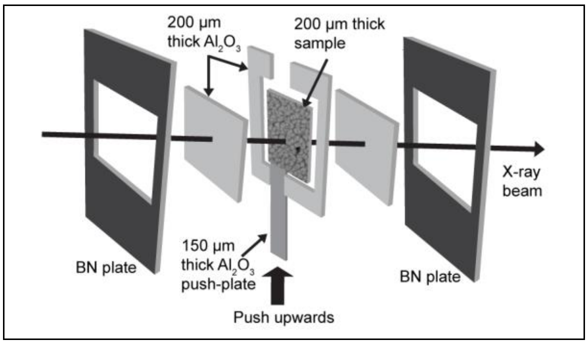

Figure 1: Schematic illustration of the direct shear experiment on Al-8Cu-0.05Ti-0.01B alloy [18]

$$\langle g_S \rangle_A = \left\langle \frac{\ln I_{SL} - \ln I_L}{\ln I_S - \ln I_L} \right\rangle_A \quad (1)$$

where A is the averaging area equal to the field of view. The mean grain size of the semi-solid alloy, $\bar{d}$, was ~130 μm (52 pixels) using the linear intercept method [27] on radiographic projection images. Time-series radiography datasets were then analysed using digital image correlation (DIC) software DaVis 8.3 developed by LaVision Imaging Company, Göettingen, Germany. The subset size for correlation was 105 × 105 pixels, whose side length equals to the nearest odd integer of $2\bar{d}$. The calculation step size, which is the spacing of two neighbouring calculation points, is 26 pixels equivalent to the nearest integer of $0.5\bar{d}$. Strain fields were derived from the sum of displacement vectors from the correlation of two consecutive images.

The grain assembly for DEM simulations was generated as follows: first the grain size and shape distributions were obtained by picking 120 grains from a radiograph prior to deformation, and the perimeter of each grain was fitted with a least-square ellipse as shown in Figure 2(a-b). Each fitted ellipse was further simplified as two overlapping circles (Figure 2(c)), in which the diameter of each circle is the short axis of the ellipse, and the distance between the centres of two circles, d_{cent}, is the difference between the long and short axes of the ellipse. 20 grains with different circle diameter and centroid distance between two circles were generated to recreate a grain assembly (Figure 2(d)) in the DEM package PFC2D Ver. 5.0 (Particle Flow Code in two dimensions) developed by Itasca Consulting Group, Inc., and the volume fraction for each template followed the grain size distribution in the experiment. The whole grain assembly was constrained by a flexible membrane boundary simplified from reference [28], which was composed of an array of circles with parallel bonds between two circles (Figure 2(e)). A constraint force was set to act on a membrane grain if the grain started to displace outward as illustrated in Figure 2(f-g). Parameters used in the simulation are summarised in Table 1, and a specific force-overlap relationship was used in this simulation to consider the occurrence of plastic deformation, as shown in Figure 3.

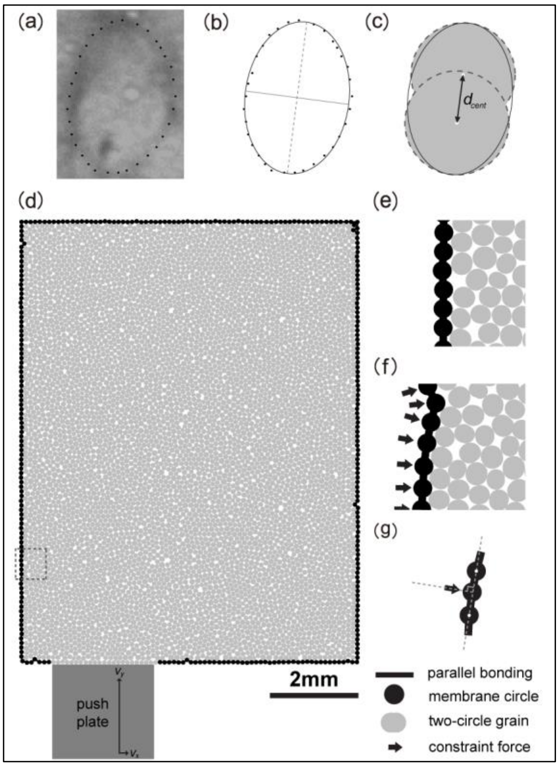

Figure 2: Schematic illustration of the DEM simulation setup: (a) typical grain from experiment, (b) fitting by an ellipse, (c) simplification from an ellipse to a two-circle grain, (d) creation of a grain assembly with size 10.4 mm × 7.9 mm ($80\bar{d} \times 60\bar{d}$). (e) is the cropped region from the dash-line square in (d) showing the undeformed configuration. (f) is the deformation microstructure after a displacement of push plate $u_y = 10\bar{d}$. Constraint force normal to the membrane was applied as the membrane boundary deformed, and (g) is the determination of normal force direction.

Table 1: Parameters used in the DEM simulation

Property	Unit	Value
Grain density, ρ	kg m^{-3}	2700
Mean circle diameter, $\bar{d}_{circle}$	μm	125
Mean centroid dist. b/t circles, $\bar{d}_{cent}$	μm	11
Elastic normal stiffness, k_n	N m^{-1}	2×10^{-2}
Elastic shear stiffness, k_s	N m^{-1}	1×10^{-2}
Normal force on membrane, F_n	N	5×10^{-9}
Friction coefficient, μ	–	0.05
Rolling friction coefficient, μ_r	–	0.5

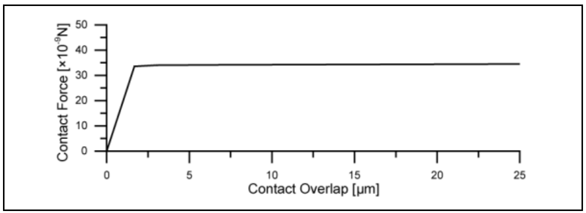

Figure 3: Normal force-overlap relationship used in the DEM simulation.

To compare the experimental and simulated mechanical response, the DEM simulation results were plotted in MATLAB (Mathworks, Natick, MA, USA), and DIC analysis was conducted on the random greyscale coloured grain assembly using a subset size of $2\bar{d}$ and step size of $0.5\bar{d}$.

3. Results and Discussion

3.1 Microstructure evolution during deformation

The semi-solid microstructure prior to deformation in the experiment is shown in Figure 4(a). The liquid in the experiment is darker than the solid phase. The distribution of grains is nearly homogeneous and has a mean solid fraction of 0.66 using Equation 1. Some black spots corresponding to a lower X-ray transmission intensity than the liquid are due to X-ray diffraction. The key grain scale phenomena that occurred in the experiments are overviewed in Figure 4(b). In region A, the grains move closer together and expel some interstitial liquid leading to compaction of the grain assembly, and some grains are plastically deformed. In region B, the grains move apart and liquid is drawn-in to the expanding interstices, leading to shear-induced dilation of the grain assembly.

Figure 5(a) shows the initial field of view in the experiment before deformation and Figure 5(b) shows the microstructure after a $10\bar{d}$ increment of Al_2O_3 push-plate motion. It can be seen that a darkened region appears which can be attributed to an increase of liquid as the grain assembly dilated. On the other hand, a high solid fraction zone in front of the push plate developed from compaction and plastic deformation of the solid grains and expulsion of some interstitial liquid.

Figure 5(c) is the initial grain assembly used in the simulations where both grains (light grey) and interstitial spaces (dark grey) are homogeneously distributed. After the horizontal and vertical increments of simulated push plate displacement, the grain assembly was deformed as shown in Figure 5(d). It can be noted that the compaction of solid grains ahead of the push plate can be clearly seen in both Figure 5(b) and 5(d), and the band of liquid enrichment in Figure 5(b) and interstitial spaces in Figure 5(d) tend to enclose the compacted solid grain area. Also, the individual grains are highly deformed near the front of the push plate, while the region farther from the push plate as well as the bottom-right edge (the free surface) are largely undeformed and underwent rigid-body displacements. On the other hand, because the DEM simulation is two-dimensional and did not include the behaviour of the liquid phase, the phenomenon of liquid flowing into the dilating space and the draining of liquid phase in the farther right-hand part were not reproduced in the particulate DEM simulation.

3.2 Quantification of strain localisation

Figures 6(a-d) show the distribution of divergence $\varepsilon_{xx}+\varepsilon_{yy}$ and shear strain ε_{xy} derived from DIC after $10\bar{d}$ increments of push-plate motion. It is clear that a strain field with negative divergence <-0.1 was developed in front of the push plate both for the experiment (Figure 6(a)) and

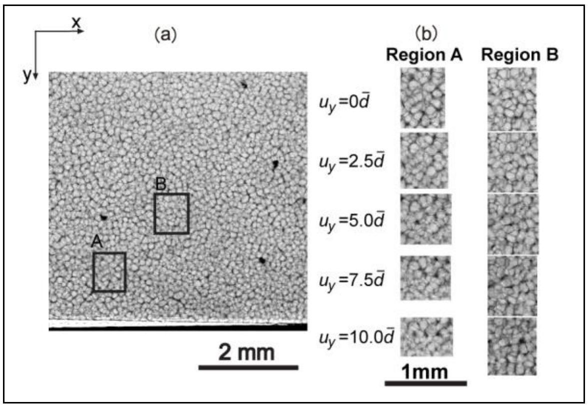

Figure 4: (a) semi-solid microstructure prior to deformation. Two regions in radiograph were selected for detailed observation in order to gain insights on strain localisation. (b) are cropped radiographic images.

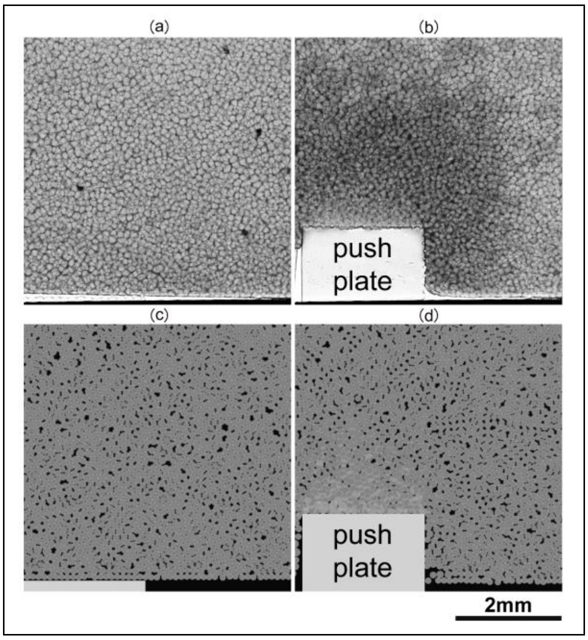

Figure 5: (a-b) Radiographs of globular Al-8Cu (a) prior to deformation and (b) deformation with push-plate displacement $u_y = 10\bar{d}$. (c) is the grain assembly created in the DEM code PFC (e.g., Figure 2), cropped to a region corresponding to the field of view in the experiment, and (d) is the simulated deformation microstructure with push-plate displacement $u_y = 10\bar{d}$.

simulation (Figure 6(b)). As the initial volume fraction (3D) of solid for the experiment is 0.66 and near to the random close packing limit of equiaxed granular materials

[29-31], the further development of local compaction in response to the displacement of the push plate occurred by individual crystal deformation. In the DEM simulation the plasticity of grains has been captured (Figure 3), so the compaction ahead of the push plate also developed as shown in Figure 6(b).

For the quantification of the dilation region (i.e., positive divergence) on X-ray images shown in Figure 6(a), however, is only localised near the top-right corner of push plate and does not cover the whole darkened region in Figure 5(b). The main reason is the occurrence of out-of-plane displacement and z-axis elongation as DIC was

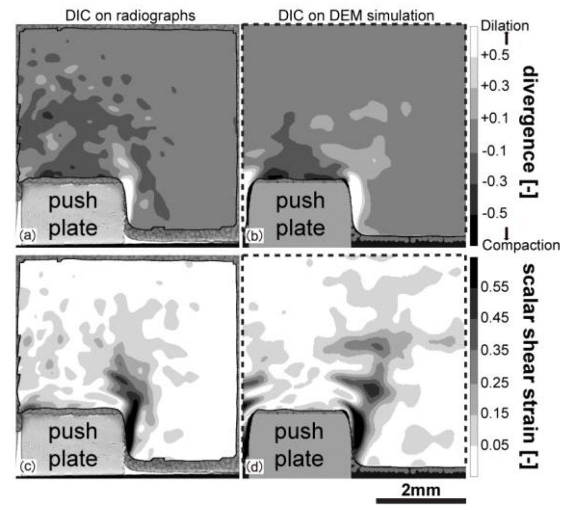

Figure 6: (a-b) divergence (ε_{xx}+ε_{yy}) mappings derived from DIC on (a) time-series radiographs and (b) plots of DEM simulation deformation microstructure. Positive divergence is equivalent to dilation. (c-d) are the mappings of scalar shear strain $|\varepsilon_{xy}|$ derived from DIC on (c) time-series radiographs and (d) plots of DEM simulation deformation microstructure. The edge of the correlation region is indicated by the solid black line, while the dashed black line represents the cropped of correlation region.

conducted on 2D projection images. In addition, the reduction of transmitted X-ray intensity by liquid enrichment shown in Figure 5(b) is not captured as DIC tracks the displacement of morphology rather than intensity change. However, it is interesting to note that the positive div-ergence in the simulation (Figure 6(b)) is clearer than in the experiment and approximately aligns along the parting plane. Future work will use an X-ray intensity approach to study the changing solid fraction field.

Figure 6(c) shows that the scalar shear strain $|\varepsilon_{xy}|$ field in the experiment contains a shear band ahead of the top-right corner of the push plate after $10\bar{d}$ displacement. The $|\varepsilon_{xy}|$ in the core part of the shear band is more than 0.35, which can be compared to the region with positive divergence shown in Figure 6(a). At the same time, the shear strain map from the DEM simulation (Figure 6(d)) shows a similar distinctive shear banding phenomenon, but with some secondary shear bands formed perpendicular to the main shear band.

The correlation between the positive divergence in Figures 6(a) and 6(b), and the distinctive local shear strain in Figures 6(c) and 6(d) shows that a dilatant shear band developed in the experiment and in the DEM simulation. Past research including post mortem analysis on samples which were deformed in the partially solidified state [12, 13] and in-situ observation of semi-solid deformation [15, 16, 18] have reported that the dilatant shear band width is approximately equal to $10\bar{d}$. The accumulated divergence and shear strain maps in Figure 6 show a similar value of shear band width based on the measurement method proposed in reference [18].

4. Conclusion

Time-resolved synchrotron X-ray imaging and the particulate discrete element method (DEM) have been applied for the investigation of semi-solid alloy deformation. The evolution of the compaction zone ahead of the push plate was reproduced in DEM with consideration of the plastic deformation of grains. Moreover, the occurrence of shear-induced dilation in both the experiment and simulation and reasonable consistency of the strain fields suggest that DEM is a well-suited model for semi-solid alloy deformation and can offer insights into the mechanical response of partially solidified alloys in pressurised casting processes.

Acknowledgements

Experiments were conducted at the SPring-8 Synchrotron on BL20B2 under Proposal No. 2015A1318. Analysis was carried out under the EPSRC Grant EP/K026763/1. T.C. Su gratefully acknowledges a President's scholarship from Imperial College London.

References

1. N.L.M. Veldman *et al.*, *Metall. Mater. Trans. A*, 2001, **32A**: 147.
2. A. Ludwig *et al.*, *Metall. Mater. Trans. A*, 2015, **46A**: 4854.
3. M.C. Flemings, *Solidification Processing*, 1974, McGraw-Hill.
4. C.P. Chen *et al.*, *Acta Mater.*, 1997, **45**: 1955.
5. S. Otarawanna *et al.*, *Metall. Mater. Trans. A*, 2010, **41A**: 1836.
6. A.B. Phillion *et al.*, *Mat. Sci. Eng. A*, 2008, **491A**: 237.
7. M. Sistaninia *et al.*, *Metall. Mater. Trans. A*, 2011, **42A**: 239.
8. M.C. Flemings, *Metall. Trans. A*, 1991, **22A**: 957.
9. H.V. Atkinson, *Prog. Mater. Sci.*, 2005, **50**: 341.
10. C. Gras *et al.*, *J. Mater. Process. Tech.*, 2005, **167**: 62.
11. Z. Bian *et al.*, *Mater. Sci. Tech-Lond.*, 2009, **25**: 599.
12. C.M. Gourlay *et al.*, *Nature*, 2007, **445**: 70.
13. B. Meylan *et al.*, *Acta Mater.*, 2011, **59**: 3091.
14. O. Reynolds, *Phil. Mag. Series 5*, 1885, **20**: 469.
15. C.M. Gourlay *et al.*, *Acta Mater.*, 2011, **59**: 4933.
16. C.M. Gourlay *et al.*, *JOM*, 2014, **66**: 1415.
17. T. Nagira *et al.*, *Scripta Mater.*, 2011, **64**: 1129.
18. T. Nagira *et al.*, *ISIJ Int.*, 2013, **53**: 1195.
19. J. Fonseca *et al.*, *Acta Mater.*, 2013, **61**: 4169.

20. T. Nagira *et al.*, *Metall. Mater. Trans. A*, 2014, **45A**: 5613.
21. K. Kareh *et al.*, *Nat. Commun.*, 2014, **5**: 7.
22. B. Cai *et al.*, *Acta Mater.*, 2016, **105**: 338.
23. C. O'Sullivan, *Particulate Discrete Element Modelling: a Geomechanics Perspective*, 2011, London: Spon.
24. C.L. Martin *et al.*, *J. Mech. Phys. Solids*, 2003, **51**: 667.
25. H.P. Zhu *et al.*, *Chem. Eng. Sci.*, 2008, **63**: 5728.
26. L. Yuan *et al.*, *Acta Mater.*, 2012, **60**: 1334.
27. ASTM E112-96, 2005, West Conshohocken, PA. pp. 267-292.
28. G. Cheung *et al.*, *Particuology*, 2008, **6**: 483.
29. C.S. O'Hern *et al.*, *Phys. Rev. E*, 2003, **68**: 011306.
30. G.Y. Onoda *et al.*, *Phys. Rev. Lett.*, 1990, **64**: 2727.
31. M. van Hecke, *Nature*, 2005, **435**: 1041.